




The numerical simulation of the post-welding stress-strain state of thin-sheets welded joints of EP718 alloy

A.Yu. Medvedev, A.E. Medvedev  , A.F. Shaikhulova , R.V. Nikiforov,
O.V. Murugova, V.R. Galimov

Ufa University of Science and Technology, Ufa, Russia

✉ medvedevandreyrf@gmail.com

Abstract. The paper presents the development of a numerical thermal deformation model of two-pass pulsed arc GMA (Gas Metal Arc) welding of a thin-sheet welded joint made of EP718 alloy using the ANSYS package, considering the distribution of temperature fields from a consumable electrode during transverse vibrations. Experimental verification of the calculation results showed that the developed thermal deformation model of two-pass GMA welding makes it possible to predict the stress-strain state of a thin-sheet welded joint with an error of 10 %, sufficient for engineering calculations. Residual stresses von Mises after welding according in the weld does not exceed 840 MPa (0.8 σ_B). The thermal deformation model of two-pass GMA pulsed arc welding developed during research can be used to assess the stress-strain state of a welded structure of complex spatial geometry with a large number of welds.

Keywords: deformation simulation during welding; heat-resistant alloy; EP718; thermal cycles during welding; ATOS deformation measurement.

Acknowledgements. Ministry of Science and Higher Education of the Russian Federation within the framework of the state assignment of “Metals and Alloys under Extreme Impacts” Laboratory of Eurasian Center of Excellence (agreement No. 075-03-2023-119/1).

Citation: Medvedev AY, Medvedev AE, Shaikhulova AF, Nikiforov RV, Murugova OV, Galimov VR. The numerical simulation of the post-welding stress-strain state of thin-sheets welded joints of EP718 alloy. *Materials Physics and Mechanics*. 2023;51(5): 79-89. DOI: 10.18149/MPM.5152023_8.

Introduction

Gas turbine engine body parts are subject to high requirements for strength and rigidity - they should provide freedom from temperature deformations of individual elements included in the body and provide simplicity and convenience in their manufacture and assembly. Usually, such highly loaded elements are made of heat-resistant nickel-based alloy KhN45MVTYuBR (EP718).

Its use for the manufacture of welded structures is complicated by the tendency to form hot cracks of various nature, not only in the weld metal, but also in the near-affected zone (NAZ), as well as grain growth and softening of the metal in the NAZ [1–8,10] One of the reasons for the increased susceptibility to cracking of the EP718 alloy in the NAZ is the high level of residual welding stresses [9]. To solve the abovementioned issues, the electron beam welding (EBW) and manual argon arc welding with a non-consumable electrode with filler wire (TIG) are used for welding the considered alloy in aircraft and engine building. The EBW technology (due to the high concentration of heat in the source) makes it possible to

form a fine-grained weld structure, but its widespread use is complicated by the following aspects: it requires laborious preparation of edges; it is difficult to apply on curved paths of welds.

Manual welding with filler material is carried out at low speeds in 3 or more passes when filling a groove with a metal thickness of 4–5 mm. This leads to repeated heating of the metal in the weld zone and the NAZ, and, as a result, the accumulation of residual stresses and an increase in the grain size. Based on the available foreign recommendations, welding of butt joints with a thickness of 4 mm from an analogue alloy of Inconel 718 can be carried out by a multilayer GMAW with a constant arc with a heat input of at least 400 kJ / m per pass of 2 mm at a welding speed of at least 24 m/h, a multilayer GMAW pulsed arc with a heat input of at least 360 kJ/m per pass of 2 mm at a welding speed of at least 15 m/h. Based on foreign data and our own experience, the use of fusion welding (consumable electrode in an inert gas) with transverse vibrations will provide a reduction in heat input up to 30 % compared to a multilayer GMAW pulsed arc, will reduce the grain growth rate, the drop in ductility in the temperature ranges of brittleness and the minimum level of residual stresses in the NAZ. When welding alloy EP718, welding wire 08Kh20N57M8V8T3R (EP533) is used. Table 1 shows the chemical composition of the EP718 alloy and EP533 welding wire [1,10,12].

It is impossible to predict residual stress and deformations of a welded assembly with many welds and with complex spatial geometry using traditional analytical calculations. The only possibility is to use powerful CAE systems, which allow simulating the stress-strain state of the welded structure after welding. The Mechanical module of the ANSYS package has this functionality.

Thus, the development of numerical models of the stress-strain state of a welded structure with complex spatial geometry after GMA welding is an urgent task, but it is extremely time-consuming and cumbersome without the stage of some simplifications. The selection of parameters of the numerical model is much easier to carry out on a somewhat simplified thermal deformation model of welding of the flat samples, which allows to quickly correct the mode parameters, followed by interpolation of the results to a more complex geometry.

Materials and Experimental methods

Material and welding technique. In the present study the base metal EP718 and welding wire EP533 alloy was used. The chemical composition of the alloy is presented in Table 1.

Table 1. Chemical composition of EP718 alloy and EP533 welding wire [1,3]

Alloys	Chemical composition, wt. %															
	C	Si	Mn	Cr	Ni	W	Mo	Mg	Nb	Al	Ti	Fe	B	P	S	Others
EP718	≤0.1	≤0.3	≤0.6	14-16	43-47	2.5-3.5	4-5.2	0.001-0.5	0.8-1.5	0.9-1.4	1.9-2.4	Remain	≤0.008	≤0.010	≤0.015	Zr≤0.02; Ce≤0.3
EP533	≤0.1	≤0.3	≤0.5	19-22	Oct.	7-9	7-9	-	-	Σ3.3	≤3.0	≤0.005	<0.015	≤0.01	≤0.1	-

The geometrical parameters of the welded joint corresponded to type C18 according to GOST 14771. Edge preparation for welding was carried out by milling. Plates with dimensions of 100 × 100 × 5 mm were welded in 2 passes by GMA-welding. Sheet blanks from the EP718 alloy had a thickness of 5 mm as delivered. Filler wire - EP533 Ø1.2 mm in hardened state. Welding was carried out with transverse oscillations of the burner relative to the weld trajectory in 2 passes. The nominal gap between the welded plates was 1.0 mm. The preparation of the edges to be welded was carried out on a milling machine. Before welding, tacking was used along the ends of the plates, followed by a selection to a height of 1.0 ± 0.5 mm.

Figure 1 shows the macrostructure of a two-pass weld made with filler wire EP533 (Fig. 1(a)), and the appearance of the front side of the weld after the first (Fig. 1(b)) and second passes (Fig. 1(c)).

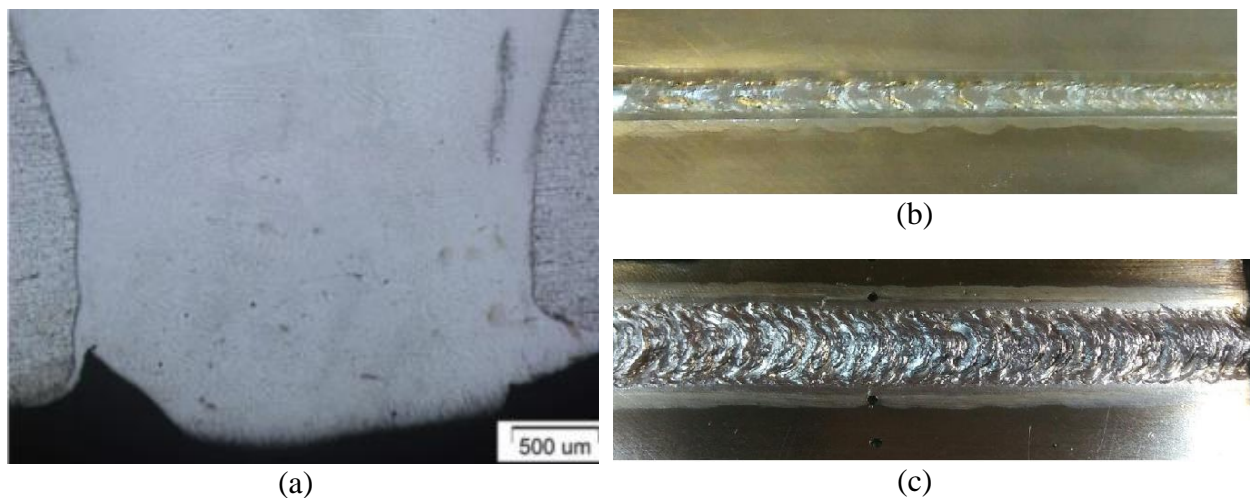


Fig. 1. Macro section of a 2-pass weld made with filler wire EP533 (a) and the appearance of the front side of the weld after the first (b) and second passes (c)

The fusion line is clearly visible on the macrostructure (Fig. 1(a)). Thanks to the use of transverse oscillations of the burner, it was possible to achieve a minimum height of the facing bead of the seam, as can be seen in Fig. 1(c). At the same time, the conducted microstructural studies and X-ray inspection of welded joints did not reveal defects in the weld and HAZ. Figure 1(a) shows the microstructure of the NAZ after the 1st pass. The microstructure of the NAZ is a partially remelted layer cold-worked as a result of milling, the grain size of which is 5–7 times smaller than the grain size of the base metal and is 5–10 μm . In this case, the length of the NAZ does not exceed 50–100 μm [20,21].

On the first pass of the weld (Fig. 1(b)), there is a large proportion of disoriented crushed structure, the presence of which can be caused using transverse oscillation technique, during which the molten metal is constantly mixed or thermomechanical vibration of the melt during pulsed arc welding. At the same time, the volume of the molten weld pool under specific conditions is significantly less than in argon-arc welding with a non-consumable electrode. In the second pass, the weld structure is more equiaxed, which is most likely due to an increase in the rigidity of the welded joint after the 1st pass and a large space for free temperature deformation between the welded edges [8,9,12].

Thermocouples were welded to the outer surface of the welded sample by capacitor welding: the first thermocouple was installed at a 1 mm from the edge, second at a 3 mm. Thermocouples were located on the line perpendicular to the joint. Thermal cycles during the welding process were recorded using a CENTER 511 digital 4-channel temperature meter. Figure 2 shows the places for installation of "K-type" thermocouples on a welded sample (Fig. 2(a)) and equipment for welding sheet blanks (Fig. 2(b)).

Longitudinal shrinkage of welded specimens was measured using the ATOS Compact Scan portable 3D scanner for full-size digitization and geometry control. ATOS is a precision measurement system for digitizing geometric objects. The measurement accuracy of ATOS Compact Scan is ≈ 0.1 mm. The measurements were taken after welding the root and facing passes.

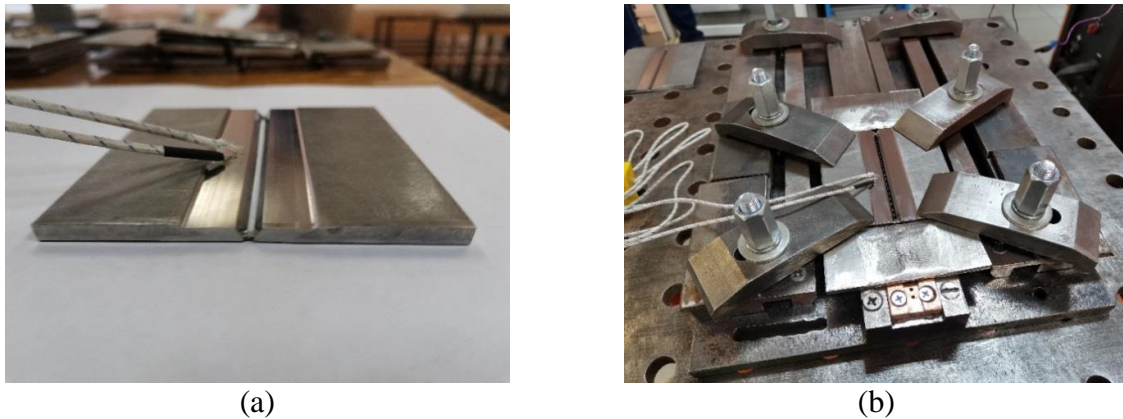


Fig. 2. Places for installation of "K-type" thermocouples on a welded sample $100 \times 100 \times 4$ mm (a) and equipment for welding sheet blanks (b)

Numerical simulation. The ANSYS/Mechanical package was chosen as a tool for numerical simulation. The calculation was carried out using the internal programming language APDL. The solution of the problem of modeling the stress-strain state of plates after welding was carried out in 2 stages: first, the thermal problem of simulating heating by a moving source was solved, and the resulting temperature field at the nodes of the model was converted into a stress and strain field at the second stage.

To describe the temperature field $T(x, y, z, t)$ in flat samples, a differential nonlinear heat conduction equation was used [3]:

$$c\rho(T)\frac{\partial T}{\partial t} = \frac{\partial}{\partial x}\left(\lambda\frac{\partial T}{\partial x}\right) + \frac{\partial}{\partial y}\left(\lambda\frac{\partial T}{\partial y}\right) + \frac{\partial}{\partial z}\left(\lambda\frac{\partial T}{\partial z}\right), \quad (1)$$

where $\rho(T)$ is the density, kg/m^3 .

The dependence of the thermophysical properties of steel on temperature $\rho(T)$, $\lambda(T)$, $c(T)$ was taken in accordance with the calculations of the OPENCALTHAD program for the average chemical composition of the EP718 alloy, since there is no information on the properties of the alloy in the scientific literature. At temperatures above 1200°C , the internal ANSYS algorithm approximates linearly the values of the property function over the last temperature interval.

The 3D model of the simulated sample consisted of two parts. First part is a plate with the size of $100 \times 100 \times 4$ mm having a groove of 30° of incline. Underneath it a copper lining is placed with a size of $100 \times 30 \times 6$ mm, having a groove of 6 mm width and 1 mm depth. Element type - Solid 70, 8-node hexahedral. The size of the finite elements near the joint is 0.3 mm, gradually increases from 1.3 to 7 mm towards the ends of the plate.

The boundary conditions for heat transfer were set from the outer and inner surfaces of the plate. Heat radiation was calculated by the equation (2):

$$q_{2r}(T) = \varepsilon C_0(T^4 - T_C^4), \quad (2)$$

where C_0 is the Stefan-Boltzmann constant, $C_0 = 5.67 \times 10^{-8} \text{ W}/(\text{m}^2\text{deg}^4)$; ε is the integral coefficient of radiant heat transfer of nickel; T is the body surface temperature, $^\circ\text{C}$; T_C is the ambient temperature, $^\circ\text{C}$.

Convective heat transfer was determined by the equation (3):

$$Q(T) = Ah(T - T_C), \quad (3)$$

where Q is the heat flux density during convection, W/m^2 ; h is the heat transfer coefficient, $\text{W}/\text{m}^2\text{ }^\circ\text{C}$; A is the surface area, m^2 ; T – body surface temperature, $^\circ\text{C}$; T_C – ambient temperature, $^\circ\text{C}$. The coefficient of convective heat transfer was determined according to the data of [11] following the dependence: $h = 0.68 \cdot 10^{-2}T$ at $0 < T < 500^\circ\text{C}$ and $h = 0.231T - 82.1$ at $T > 500^\circ\text{C}$. The initial temperature T and the ambient temperature T_C were set to be 20°C in the calculations.

The boundary conditions of the contact "weld sample - copper lining" were considered as the sum of thermal conductivities of the air gap α_{air} between the microprotrusions of the contacted materials and the metal contact α_M . As a result of calculations, the following values of contact thermal conductivity $\alpha_{\text{air}}(T)=9100 + 28T$ were obtained [8].

The welding mode parameters were taken from full-scale experiments. During the welding of the root pass, the heat input was 147 kJ/m, during the welding of the facing pass, it was 150 kJ/m [4-8]. To model the heating source, the Goldak double semi-ellipsoid model was used, the scheme of which is presented in Fig. 3 [8,9].

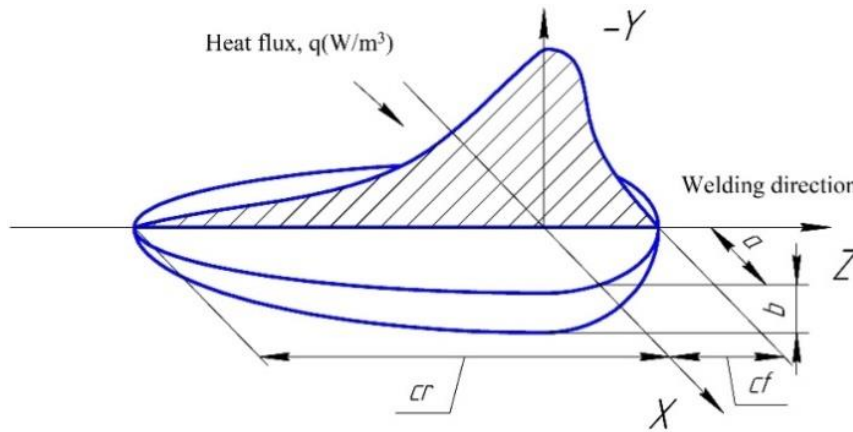


Fig. 3. Goldak's double semi-ellipsoid model [8,9]

For a point inside the first semi-ellipsoid, located in front of the weld pool, the heat flux was determined by the equation (4):

$$q(x, y, z) = \frac{6\sqrt{3}(f_f Q)}{abc_f \pi \sqrt{\pi}} \exp\left(\frac{-3x^2}{a^2} - \frac{3y^2}{b^2} - \frac{3z^2}{c_f^2}\right), x \geq 0, \quad (4)$$

where f_f is the part of the heat flow in the front part of the bath; a , b , c are the semi-axes of the ellipsoid.

For points (x, y, z) inside the second semi-ellipsoid at the back of the weld pool, the heat flux was described by the equation (5):

$$q(x, y, z) = \frac{6\sqrt{3}(f_r Q)}{abc_r \pi \sqrt{\pi}} \exp\left(\frac{-3x^2}{a^2} - \frac{3y^2}{b^2} - \frac{3z^2}{c_r^2}\right), x < 0, \quad (5)$$

where f_r is the heat flow to the back of the weld pool.

In the calculations, $f_f/f_r = 1/3$ was taken, and the effective heating efficiency was taken as 0.8.

The specific heat flux was adapted to the equation of uniform motion along a sinusoid, simulating the transverse vibrations of a welding torch:

$$q = Q \cdot \exp\left(-3 \left(\left(\frac{Z-v \cdot t}{r_1} \right)^2 + \left(\frac{Y}{r_2} \right)^2 + \left(\frac{X-T \sin(A \cdot t)}{r_3} \right)^2 \right) \right), \quad (6)$$

where Q is the input power, W; t is the time, s; V is the source velocity, m/h; r_i – ellipsoid semi-axes, m; T – period, s^{-1} ; A is the amplitude, mm. The values of $T=1.5$ mm and $r=2.2$ mm were taken.

Results and Discussion

Analysis of the simulation results. Figure 4 shows the distributions of temperature fields from a movable heating source of the type of a double Goldak's semi-ellipsoid. Verification of the results of simulation of the thermal problem during welding was carried out by comparing thermal cycles from the nodes of the finite element mesh, corresponding to the places where "K-type" thermocouples are fixed on the welded sample, as shown in Fig. 2.

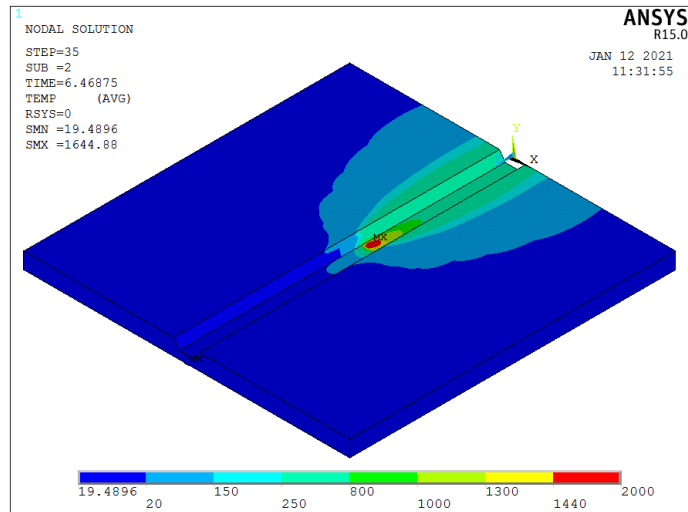
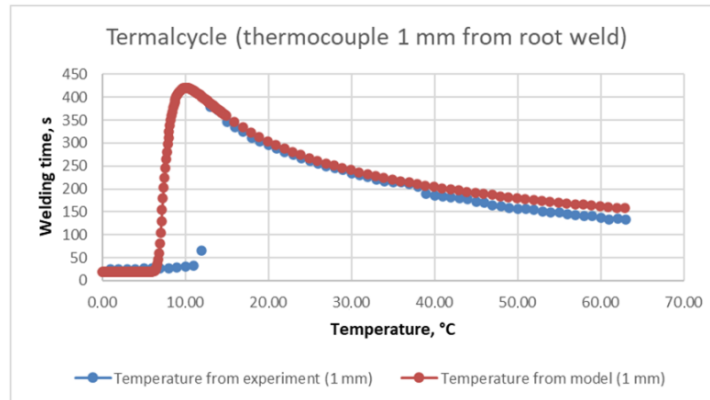
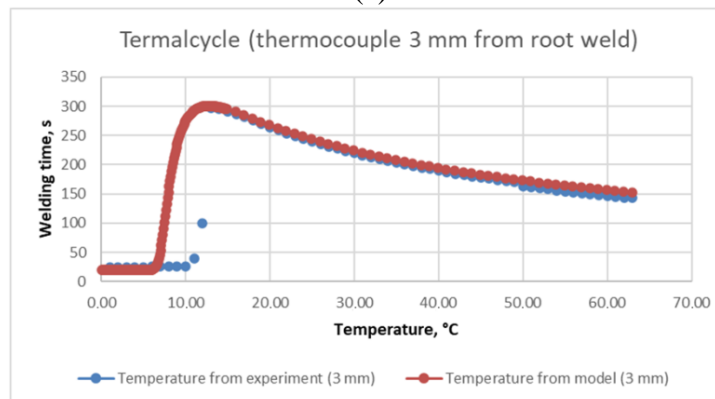


Fig. 4. Distributions of temperature fields from a moving source heating type double semi-ellipsoid Goldak: 1st pass: $t=6,47$ s



(a)



(b)

Fig. 5. Thermal cycles from thermocouples No. 1 at 1 mm (a) and 3 mm (b) for root

Figure 5 shows thermal cycles from thermocouples and nodes of a finite element mesh during simulation after the first welding pass, a detailed analysis of thermal cycling of welded specimens is presented in [5,6].

The thermal cycles from the numerical thermal model of welding reflect the actual heating during 2-pass fusion welding of the EP718 alloy with an error of no more than 7 % compared to the experimental data.

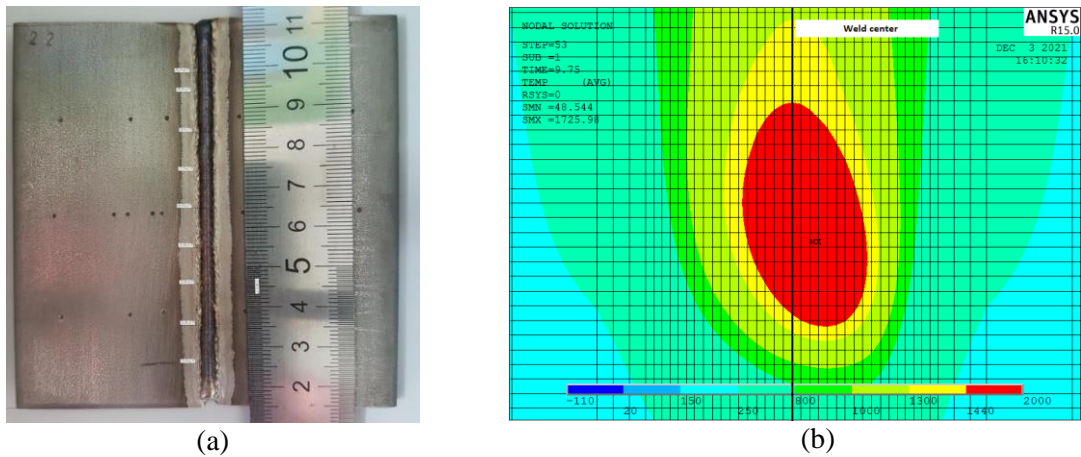


Fig. 6. The width of the weld after a two-pass GMA-welding with transverse vibrations (a) and an example of the penetration zone when modeling the second weld of a GMA-welding with transverse vibrations (b)

Figure 6 shows the measurement of the width of the penetration zone after the second pass of the robotic GMA-welding by measuring the dimensions and bringing them to the desired scale in the KOMPAS 3D program using 9 points along the axis of the weld.

As shown in Fig. 6(b), the width of one element in the weld zone is 0.46 mm, as the source advances to the melting temperature, the conditional weld zone heats up by 15.5 elements in width, which corresponds to 7.13 mm in the width of the penetration zone.

Figure 7 shows a range graph comparing the results of measuring the width of the penetration zone for samples after statistical processing using the least squares method along the median with significance quantiles Q25 % and Q75 %.

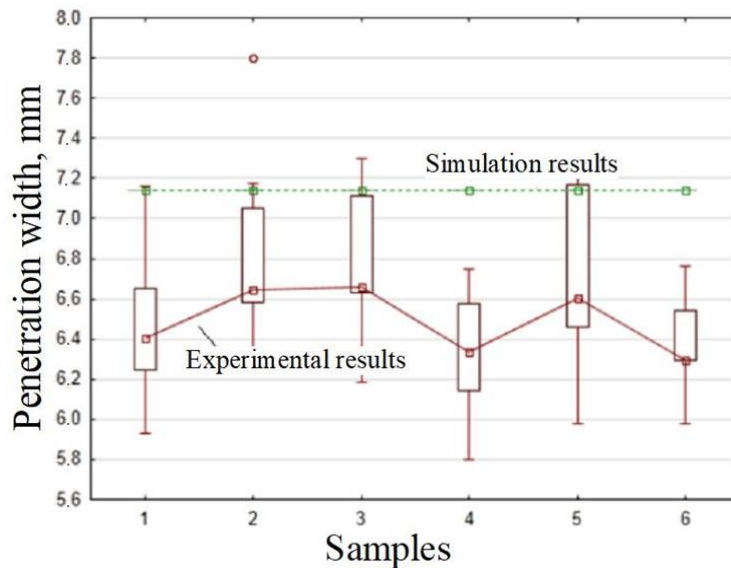


Fig. 7. Range diagram of weld width measurement results

As the comparison of the experimental and modeling data in Fig. 1 demonstrates, the developed numerical temperature model of the 2-pass GMA-welding of the EP718 alloy makes it possible to predict the size of the penetration zone with an error of 9 % compared to the experimental data.

Welded joint deformation and stress analysis. A mathematical model of plasticity behaviour with isotropic hardening (MISO) was used. The mechanical properties were taken according to the OPENCALTHAD method data on the average chemical composition of the EP718 alloy and EP533 wire, since there is no information on the mechanical properties of the alloys in the scientific literature. However, the simulated mechanical properties are almost identical to those of Inconel 718 [14,16–19,24].

The strain hardening curves modeled for the EP718 alloy using the OPENCALTHAD method, are almost identical to the strain hardening curves of the Inconel 718 alloy presented in [11,13].

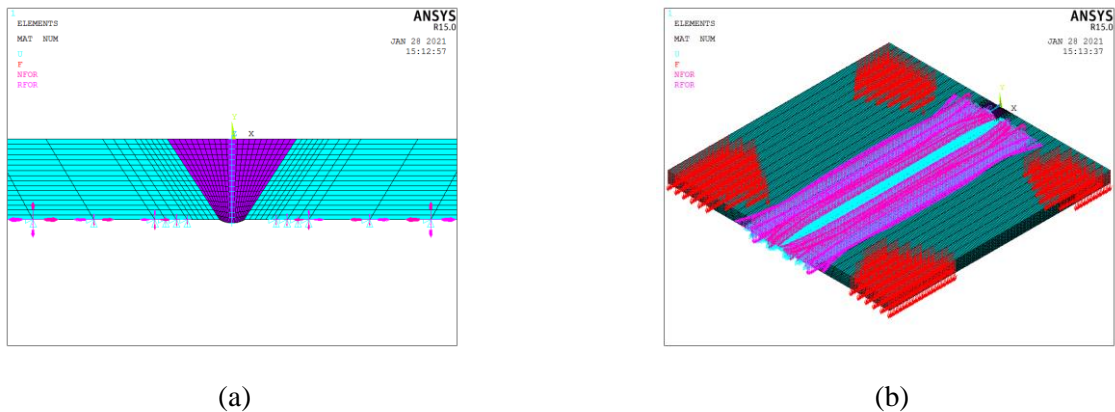


Fig. 8. Fixing a 3D model for calculating the stress-strain state after robotic consumable electrode welding: (a) Fixing along the OX and OY axes, (b) Imitation of clamps for clamping a sample in a tooling

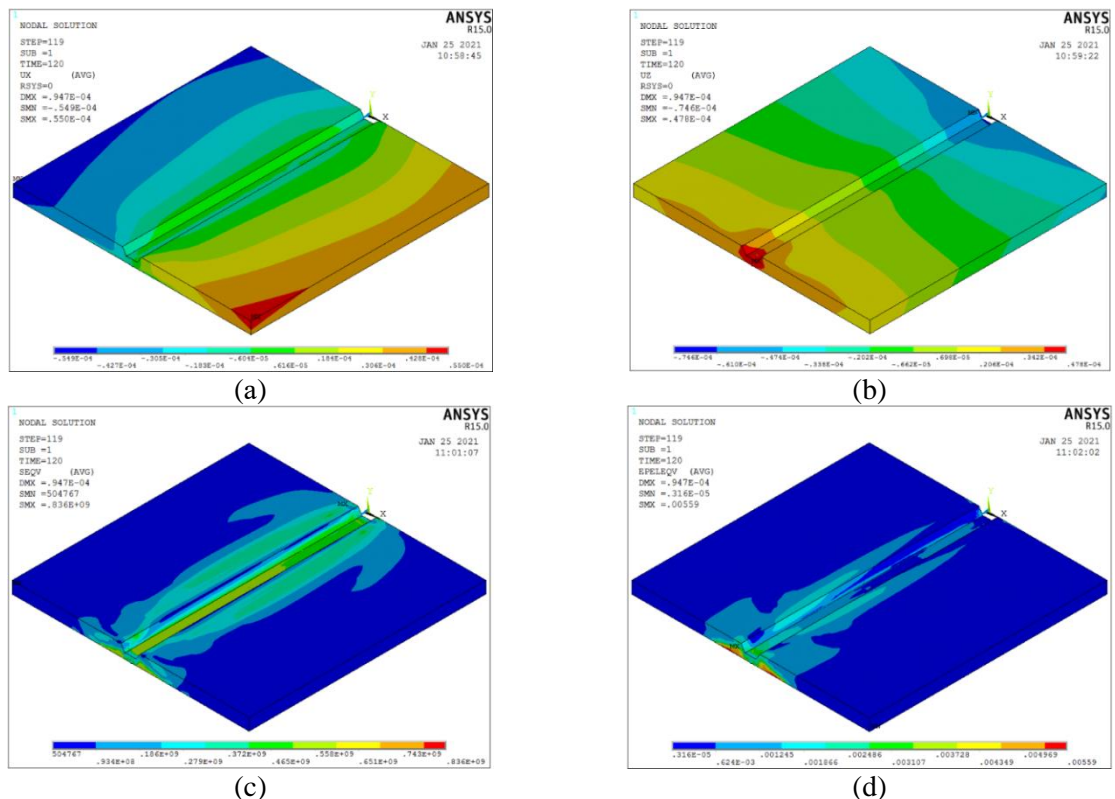


Fig. 9. The results of simulation of displacements (a,b) and residual welding stresses (c,d) during GMA welding of the butt joint of EP718 alloy after the 1st pass

The scheme of fixing the plate in the tooling for calculating deformations is presented in Fig. 8. Fastening along the OX axis is carried out by fixing the movements of nodes along the line in the middle of the plate; along the OY axis – by supporting along the area of contact of the sample with a copper lining and by applying the force of ≈ 20 kg for each of the 4 clamps (200 N / number of nodes on the surface). Figure 9 shows the results of modeling the stress-strain state of butt joints from sheet EP718 after the 1st pass.

The simulation results are summarized in Table 2. After the first pass, the equivalent stress level is 836 MPa ($\approx 0.6 \sigma_B$) and decreases to the level of 783 MPa ($\approx 0.56 \sigma_B$), while the transverse shrinkage increases to 0.055 from 0.157 mm after the first pass, which is primarily caused by an increase in the stiffness of the samples after the first pass and the heat input during welding, as well as a decrease in the free volume for plastic deformation between the edges in the second pass. The level of plastic deformation increases from 0.0056 to 0.063 % also due to an increase in the heat input during welding.

Table 2. Simulation results of the stress-strain state of butt joints made of sheet EP718

Condition	Transverse shrinkage, mm	Longitudinal shrinkage, mm	Maximum equivalent stresses, MPa	Maximum equivalent strains, %
After first pass	0.055	0.048	836	0.0056
After second pass	0.157	0.125	783	0.063

Verification of the deformation problem using ATOS. The verification of the stress-strain model (section 3.3) was performed using the ATOS. The ATOS system is a coordinate-measuring topometric system for determining the geometric parameters of surfaces of complex shape. One of the samples with marking points in the ATOS Compact Scan system is shown in Fig. 10(a) - the displacement of points corresponds to the transverse shrinkage of the sample. Figure 10(b) demonstrates a 3D model in ANSYS with points corresponding to the location of the markings on the welded samples.

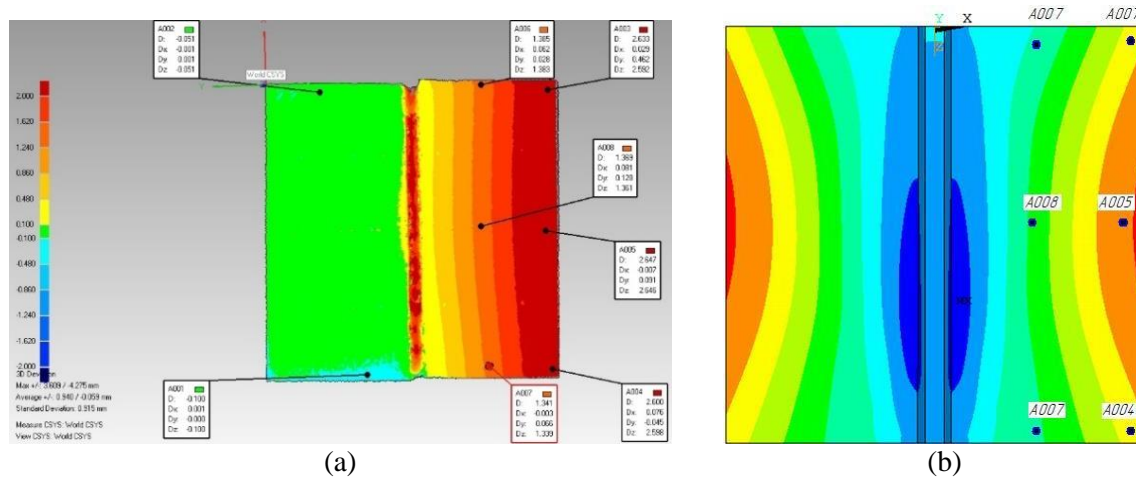


Fig. 10. Movement of points on the outside of the weld after the second pass, measured with ATOS (a) and the corresponding points on the 3D model in ANSYS (b)

The developed numerical thermal deformation model of 2-pass GMA-welding of the EP718 alloy makes it possible to predict deformations with an error of no more than 10% compared to experimental data. And the mechanical properties in the elastic and plastic deformation region for EP718 alloys and EP533 wire, modelled by the OPENCALTHAD method, are suitable for use in the developed thermal deformation model [11,13].

In a number of studies, the same 3D scanning method was used with the ATOS 2 system to evaluate the deformations of welded joints of bimetals obtained by explosion

welding (EXW). Data analysis showed that the scanning accuracy is sufficient not only to assess not only the deformations of welded joints, but also to detect external defects with a size of 0.25 mm [14]. The paper [15] considers the 3D scanning method as one of the options for assessing the deformation of welded joints obtained by arc welding methods - TIG / GMA. However, there are no data on measurement errors in the work.

Verification of the thermal and deformation models with sufficient accuracy for engineering calculations provided the formation of a knowledge base for finite element modeling of the thermal deformation state of a flat sample during and after robotic welding, which makes it possible to synthesize a similar welding model of a real aircraft engine assembly with a large number of welds.

Conclusions

1. A thermal model of welding has been developed that reflects the actual heating during 2-pass fusion welding of butt-welded joints 4 mm thick from the EP718 alloy with transverse oscillations of the burner with an error of no more than 7 % compared with the experimental data.
2. A thermal deformation model of 2-pass GMA-welding of EP718 alloy of 4 mm thick butt-welded joints with transverse torch oscillations was developed, which makes it possible to predict deformations with an error of no more than 10% compared with experimental data. Verification of residual deformations of welded samples was carried out using the ATOS system.
3. Based on the results of numerical simulation of 2-pass GMA-welding of butt-welded joints 4 mm thick from alloy EP718, it was found that the level of equivalent residual stresses according to von Mises in the weld does not exceed 840 MPa ($0.8 \sigma_B$).
4. The thermal deformation model of 2-pass GMA-welding developed during research can be used to assess the stress-strain state of a welded structure of complex spatial geometry with a large number of welds, provided that the parameters of the heating source and the parameters of the finite element mesh of the 3D model of the structure are constant.

References

1. Sorokin LI. Filler materials for welding heat-resistant nickel alloys (review). Part 1. *Welding Production*. 2003;4: 4-16. (In-Russian)
2. Agilan M, Krishna SC, Manwatkar SK, Vinayan EG, Sivakumar D, Pant B. Effect of Welding Processes (GTAW & EBW) and Solutionizing Temperature on Microfissuring Tendency in Inconel 718 Welds. *Materials Science Forum*. 2012;710: 603–607.
3. TU 14-1-1059-74. *Sheets from alloy grades KhN45MRTYBR-VD(EP718-VD), KhN45MVTYBR-ID(EP718-ID). Specifications*. (In-Russian)
4. Nikiforov RV. *Improving the technology of TIG-welding of butt joints from thin-sheet corrosion-resistant steels, taking into account thermal deformation processes in the product*. *Cand. Tech. Sciences Thesis 05.02.10*. Moscow; 2014. (In-Russian)
5. Atroshchenko VV, Nikiforov RV, Murugova OV. Development of technology for robotic consumable electrode welding of KhN45MVTYBR alloy joints. *Welding and Diagnostics*. 2020;4: 46–49. (In-Russian)
6. Medvedev AU, Nikiforov RV, Galimov VR, Murugova OV, Savichev MP, Bolshakov BO. Peculiarities of the formation of the near-weld zone microstructure during robotic welding of a heterogeneous nickel-based alloy. *Materials. Technologies. Design*. 2021;3(1): 40–47. (In-Russian)
7. Nikiforov RV, Murugova OV. Application of robotic GMA-welding for nickel alloys in aircraft engine building. *Youth Bulletin of USATU*. 2020;1(22): 109–111. (In-Russian)
8. Nikiforov RV, Murugova OV. Analysis of residual stresses after welding of structures of complex spatial geometry with curved trajectories of welds. *Youth Bulletin of USATU*. 2020;2(23): 101–105. (In-Russian)

9. Deng D, Murakawa H. Numerical simulation of temperature field and residual stress in multi-pass welds in stainless steel pipe and comparison with experimental measurements. *Computational Materials Science*. 2006;37(3): 269–277.
10. Sorokin LI. On the formation of hot cracks in the seam at welding of heat-resistant alloys. *Welding Production*. 1997;4: 12–18. (In-Russian)
11. John N. DuPont, John C. Lippold, Samuel D. Kiser. *Welding metallurgy and weldability of nickel-base alloys*. A John Wiley & Sons Inc.; 2009.
12. Sorokin LI. Stresses and cracks during welding and heat treated heat resistant nickel alloys. *Welding Production*. 1999;12: 11–16. (In-Russian)
13. Ramkumar KD, Mulimani SS, Ankit K, Kothari A, Ganguly S, Effect of grain boundary precipitation on the mechanical integrity of EBW joints of Inconel 625. *Materials Science and Engineering: A*. 2021;808: 140926.
14. Jerold JP, Dev AM. Comprehensive Analysis of TIG Welded Inconel–718 Alloy for Different Heat Input Conditions. *International Journal of Engineering and Technology*. 2018;(3.6): 206–209.
15. Urminsky J, Marônek M, Jáňa M, Morovič L. Analysis of Weld Joint Deformations by Optical 3D Scanning. *Acta Polytech*. 2016;56(1): 76–80.
16. *The ABC's of Arc Welding and Inspection*. Tokio, Japan: Kobe Steel, LTD; 2011.
17. Benoit A, Jobez S, Paillard P, Klosek V & Baudin T. Study of Inconel 718 weldability using MIG CMT process. *Science and Technology of Welding and Joints*. 2011;16(6): 477–482.
18. Isaev LS. Simulation of heat transfer processes during laser welding of dissimilar metals using an intermediate insert. *Bulletin of Samara State Technical University. Technical Sciences*. 2016;4(52): 123–129. (In-Russian)
19. Brochu M. Thermal stability of a Stellite/steel hardfacing interface during long-term aging. In: *Proc. of 13th International Conference on Fracture, Beijing, China, June 16-21, 2013*. 2013. p.1–10.
20. Gregori A. Welding and Deposition of Nickel Superalloys 718, Waspaloy and Single Crystal Alloy CMSX-10. *Welding in the World*. 2007;51(11–12): 34–47.
21. Devendranath Ramkumar K, Jagat Sai R, Santhosh Reddy V, Gundla S, Harsha Mohan T, Saxena V, Arivazhagan N, Effect of filler wires and direct ageing on the microstructure and mechanical properties in the multi-pass welding of Inconel 718. *Journal of Manufacturing Processes*. 2015;18: 23–45.
22. Tkacheva AV, Abashkin EE. Impact of forced cooling of the joint zone and thermal effect on the distribution values of residual stress generated by arc welding. *Materials Physics and Mechanics*. 2022;50(3): 509–517.
23. Mimmi A, Merzoug M, Ghazi A, DellalN. Mechanical behavior of structures welded with friction stir lap welding process. *Materials Physics and Mechanics*. 2023;51(2): 151–163.

THE AUTHORS

Medvedev A.Yu.

e-mail: medvedev.ayu@ugatu.su

Medvedev A.E. 

e-mail: medvedevandreyrf@gmail.com

Shaikhulova A.F. 

e-mail: shaiulova@inbox.ru

Nikiforov R.V.

e-mail: nikiforov_svarka@mail.ru

Murugova O.V.

e-mail: murugova.oxana@mail.ru

Galimov V.R.

e-mail: houndedreaper@mail.ru